Available online at www.sciencedirect.com

C. R. Physique 6 (2005) 89–103

http://france.elsevier.com/direct/COMREN/

Self-organization on surfaces/Auto-organisation sur les surfaces

Three-dimensional stacking of self-assembled quantum dots in multilayer structures

Gunther Springholz

Institut für Halbleiter- und Festkörperphysik, Johannes Kepler Universität Linz, A-4040 Linz, Austria

Available online 13 January 2005

Presented by Guy Laval

Abstract

Three-dimensional stacking of semiconductor nano-islands in multilayers or superlattice structures provides a powerful tool for controlling the properties of self-assembled quantum dots. These stackings can be caused by several different mechanisms based on: (i) elastic interactions due to the strain fields of the buried dots; (ii) morphological interactions due to nonplanarized spacer topographies; or (iii) interactions based on chemical composition modulations within the spacer material. All three interactions may give rise to a vertical dot alignment in columns as well as to oblique or staggered dot stackings, depending on the details of the interaction mechanisms. For the interlayer correlations mediated by the elastic strain fields, the elastic anisotropy and surface orientation, but also the dot sizes and spacer layer thicknesses play a crucial role. As a result, transitions between different types of dot stackings can be induced as a function of spacer layer thicknesses and growth parameters. The large range of parameters involved in interlayer correlation formation may allow the controlled synthesis of new types of ordered structures with novel properties. ***To cite this article: G. Springholz, C. R. Physique 6 (2005).***
© 2004 Académie des sciences. Published by Elsevier SAS. All rights reserved.

Résumé

Empilements tridimensionnels en multicouches de boîtes quantiques auto-assemblées. L'auto-organisation tri-dimensionnelle d'îlots de matériaux semi-conducteurs par dépôt de multicouches permet de modifier substantiellement les propriétés des boîtes quantiques. Ces empilements peuvent résulter de plusieurs phénomènes (i) les déformations élastiques de la matrice résultant des contraintes liées aux boîtes (ii) des effets topographiques liés à la corrugation de la surface libre de la matrice (iii) une modulation chimique de la matrice. Ces trois effets peuvent conduire à un alignement vertical des boîtes en structures colonnaires, ou à des empilements inclinés, selon les mécanismes en jeu. En particulier, dans le cas des interactions élastiques les paramètres pertinents sont l'orientation de la surface, l'éventuelle anisotropie des propriétés élastiques de la matrice, la taille des boîtes et l'épaisseur de la matrice entre deux couches de boîtes. Des transitions entre différents types d'empilement peuvent ainsi être obtenues en jouant sur l'épaisseur des couches de matrice ou sur les conditions de croissance. La large palette d'effets mis en jeu devrait permettre la synthèse de nouveaux types de super-réseaux de boîtes, présentant des propriétés originales. ***Pour citer cet article : G. Springholz, C. R. Physique 6 (2005).***
© 2004 Académie des sciences. Published by Elsevier SAS. All rights reserved.

Keywords: Quantum dots; Stranski–Krastanow growth mode; Self-organization; Superlattices; Molecular beam epitaxy; Self-assembly

Mots-clés : Boîtes quantiques ; Croissance Stranski–Krastanow ; Auto-organisation ; Super-réseaux ; Croissance par jets moléculaires ; Auto-assemblage

E-mail address: gunther.springholz@jku.at (G. Springholz).

1631-0705/$ – see front matter © 2004 Académie des sciences. Published by Elsevier SAS. All rights reserved.
doi:10.1016/j.crhy.2004.11.001

1. Introduction

Self-assembled growth of nano-islands by strained-layer heteroepitaxy has recently evolved as an effective tool for fabrication of semiconductor quantum dots [1–4]. It is based on the natural tendency of highly strained layers to spontaneously form three-dimensional (3D) nano-islands on the surface of a uniform 2D wetting layer with monolayer thickness [5–7]. Initially, these islands are fully coherent and defect free, and only in the later stages of growth misfit dislocations are introduced for plastic strain relaxation. The driving mechanism for this Stranski–Krastanow (SK) growth transition is the highly efficient strain relaxation possible within the 3D islands due to the elastic lateral expansion or compression in the directions of the free side faces [4,5,8–11]. For islands larger than a certain critical size, the energy thus gained outweighs the corresponding increase in free surface energy, which results in a significant lowering of the total energy of the system [5,9,10]. As a consequence, this growth mode is the preferred behavior strained heteroepitaxial layers under near-equilibrium conditions, providing a tool of nanofabrication for a large variety of material systems. In particular, when the surface nano-islands are embedded in a higher energy band gap matrix material, the free carriers are confined by the surrounding barriers, thus leading to the formation of self-assembled quantum dots with atomic-like optical and electronic properties [12].

Due to the statistical nature of growth, self-assembled quantum dots exhibit a considerable variation in sizes and shapes, with a corresponding inhomogeneous broadening of the electronic density of states [1–3,12]. In addition, there is little control over the lateral arrangement and position of the nano-islands. Both factors pose significant problems for device applications. In this respect, three-dimensional stacking of self-assembled quantum dots in multilayers or superlattice structures provides a powerful tool for controlling the properties of self-assembled quantum dots [13–18,89]. This has been used not only to increase the total volume of the active material in actual devices, but also to tune the electronic wave functions due to the coupling of the quantum states across the spacer layers [18,19]. As a result, quantum dot *molecules* [19–21] can be obtained, which are of particular interest for quantum computation applications [21,22]. In addition, under certain conditions, multi-layering of nano-islands has been found to yield not only significant improvements in the size uniformity [15,16,23–26], but also allows the synthesis of ordered quantum dot superstructures [16,23]. This is due to the presence of dot interactions that induce the formation of long-range interlayer dot correlations, which, under favorable conditions, will cause a lateral ordering of the dots within the growth plane as well [15,16,23].

For different material systems, different types of vertical and lateral correlations have been observed, ranging from a vertical alignment of the dots in *columns* along the growth direction for Ge/Si [17,18,27–30] or InAs/GaAs [13,14,31–34] dot superlattices, to vertical *anti-correlations* or *fcc*-stackings for II–VI and IV–VI semiconductors [16,35–37]. The type of correlations actually formed has been found to depend on a large variety of parameters such as the spacer layer thickness [13,28,34,36,38], the dot sizes [34,39], the elastic properties of the materials [40,41], the surface orientation [40], the growth conditions [34,42] and the chemical composition of the dots and the spacer layers [43–47]. Most importantly, under certain conditions a significant lateral ordering and narrowing of the size uniformity has been obtained [16,25,38,40,43].

In the present article, the different mechanisms and the resulting different dot stackings are reviewed and discussed in detail for the prototype Si/Ge, InAs/GaAs, and PbSe/PbEuTe quantum dot material systems. From strain calculations it is shown that the elastic anisotropy and the surface orientation play a crucial role for the formation of staggered dot stackings. In addition, other mechanisms are discussed that may lead to interlayer correlations inclined stackings in multilayer structures. This may be used to tune and control the physical properties of self-assembled quantum dot systems.

2. Mechanisms for interlayer correlation formation

The formation of interlayer dot correlations in multilayer structures is caused by long-range interactions between the growing dots on the surface and those buried within the previous layers. Since once formed, self-assembled quantum dots are rather immobile due to their very rapid growth in size, these correlations must be formed at the very early stages of dot nucleation. Thus, the modification of the nucleation process is the crucial mechanism through which the buried dots act on the growth of the subsequent quantum dots. Apart from the interlayer dot correlations created during multilayer growth, the action of these interactions is also manifested by the significant changes in dot size [15,26,29,32,38,48–50], density [15,26,32,48,49], shape [28,48], lateral arrangement [15,16,25,26,48,51] as well as critical thickness for dot nucleation [52–54] as a function of the number of deposited layers, as has been observed in many experiments.

Nucleation of Stranski–Krastanow dots is obviously a very complex process that sensitively depends on many parameters such as surface stress, lattice-mismatch, chemical composition, wetting layer thickness, surface free energies, morphology and local curvature of the surface, as well as the surface step structure and surface kinetics. While on a planar and chemically uniform substrate, self-assembled Stranski–Krastanow islands nucleate randomly on the surface, in multilayer structures, the presence of subsurface nano-islands below the surface induces significant variations of these parameters across the growth front when the spacer thickness is not very large (typically of the order of the lateral dot spacing). Accordingly, new dots will nucleate

preferentially at certain surface sites that are determined by the locations of the buried subsurface dots. This heterogeneous nucleation may be driven by (i) a local increase of the growth caused by vertical or lateral mass transport, or by (ii) a local decrease of the critical island size and energy barrier for dot nucleation. As illustrated in Fig. 1, thus three basic mechanisms of how these interlayer correlations may be induced can be distinguished. These are: (i) elastic lattice deformations around the buried dots below the surface, giving rise to a nonuniform strain distribution on the surface [13,16,23,40]; (ii) corrugations in surface topography due to incomplete surface planarization during overgrowth [55]; and finally (iii) chemical nonuniformities of the growing surface caused by surface segregation or chemical decomposition of the spacer layer material [45–47]. In principle, all three mechanisms can give rise to a vertical dot alignment along the growth direction as well as to a staggered dot stacking, as is shown schematically in the top and bottom panels of Fig. 1, respectively.

Experimentally, indeed different dot stackings have been observed by for various material systems. Fig. 2 shows some representative examples as revealed by cross-sectional transmission electron microscopy (TEM). Generally, the vertical dot alignment along the growth direction is the predominant case for most self-assembled quantum dot systems as is exemplified in Fig. 2(a) for an InAs/GaAs superlattice [33]. In this material systems the interlayer correlations in columnar structures were

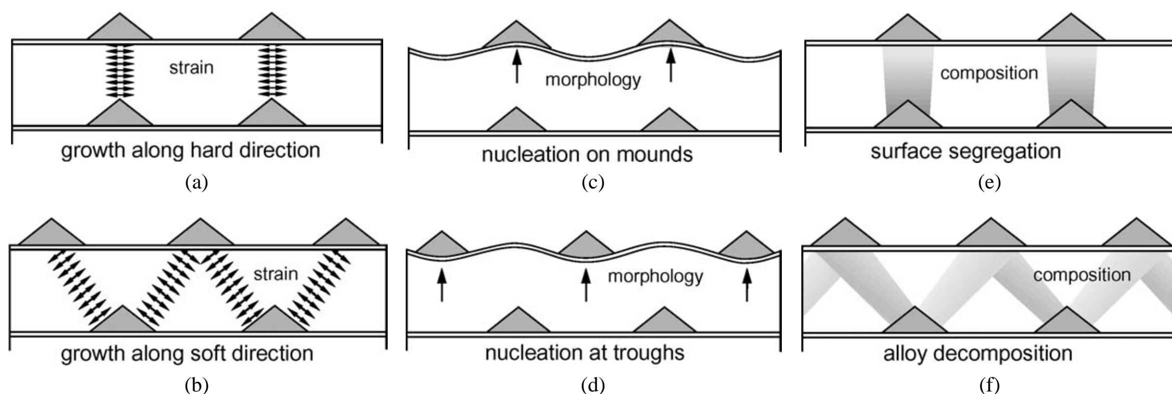

Fig. 1. Different possible mechanisms for formation of interlayer correlations in self-assembled quantum dot multilayer structures. Left-hand side: interlayer interaction mediated by the elastic strain fields of the buried dots below the surface, causing a preferential dot nucleation at the minima of the surface strain distribution. In dependence of the elastic properties as well as surface orientation, these minima can be localized above (a) or between (b) the buried dots, giving rise to a vertical alignment or staggered dot stacking. Center: interlayer correlations caused by nonplanar surface morphologies of the spacer layer above the buried islands. In dependence of the dominant mechanism of surface mass transport (capillarity (c) or stress-driven (d)), subsequent dots may nucleate either on top of the mounds above the dots (c), or in the troughs in between (d). Right-hand side: interactions caused by a nonuniform chemical composition of the spacer layer caused by surface segregation (e) or alloy decomposition (f). As indicated, by all three mechanisms, not only a vertical dot alignment (top) but also a staggered stacking (bottom) may be introduced in multilayer structures.

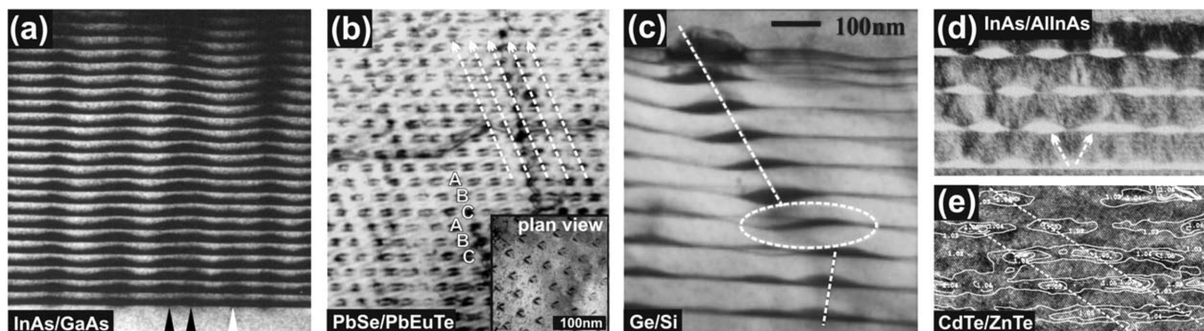

Fig. 2. Examples for different types of interlayer dot stackings in self-assembled quantum dot multilayers as revealed by cross-sectional transmission electron microscopy: (a) vertically aligned (001) InAs quantum dot superlattice with 20 nm GaAs spacer layers [32]. (b) $ABCABC\ldots$stacking in a PbSe/PbEuTe (111) quantum dot superlattice with 5ML PbSe alternating with 45 nm PbEuTe. The plan-view TEM insert shows the resulting 2D hexagonal ordering within the growth plane [16]. (c) Inclined dot correlations in a Ge dot superlattice of 1.2 nm Ge alternating with 40 nm Si spacers [55]. (d) Vertically anticorrelated InAs/AlInAs quantum wire superlattice (3ML/10 nm, respectively) on InP (001) [45,46]. (e) Anticorrelated multilayer of 2 ML CdTe islands separated by 15 ML ZnTe spacers [37]. The white contour lines indicate the iso lattice-parameters, i.e., chemical composition as extracted from the atomically resolved TEM images.

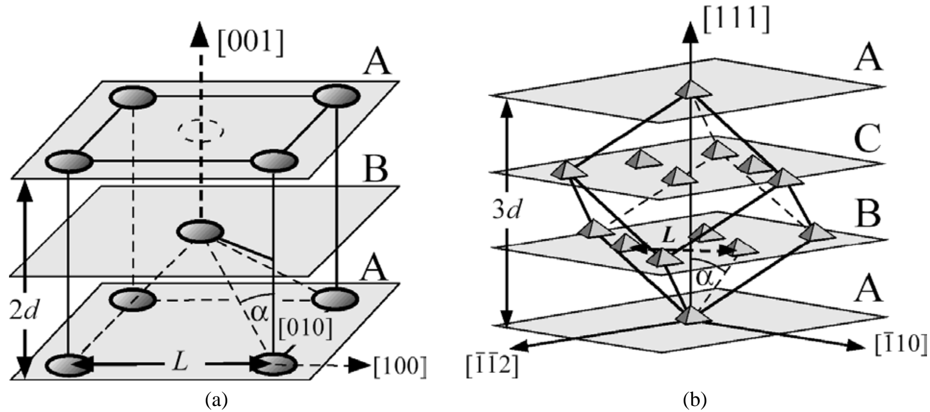

Fig. 3. Schematic illustration of the two major possible 3D dot stackings in self-organized quantum dot multilayer expected for cubic materials with high elastic anisotropy A when the growth orientation is parallel to the elastically soft direction. (a) $ABAB\ldots$ stacking and centered tetragonal dot lattice for the (100) growth orientation and $A \gg 1.5$ and (b) *fcc*-like $ABCABC\ldots$ dot stacking and resulting trigonal 3D dot lattice for the (111) growth orientation and materials with $A < 0.6$, as observed for PbSe/PbEuTe superlattices shown in Fig. 2(b). These stackings are based on the strain energy distributions shown in Fig. 3 (c) and (f), and they can be formed only when the lateral spacing of the energy minima $L_{\min}$ is significantly larger than the lateral dot sizes.

found to persist up to spacer thicknesses of about 50 nm [13,14,31–34]. A vertical dot alignment is usually found also for SiGe/Si superlattices [27–30] with spacer thicknesses up to 70 nm [28], as well as for InP/GaInP [56] and GaN/AlN [57] multilayers. On the other hand, staggered dot stackings were observed for a number of other systems such as II–VI dot superlattices [35–37] and InAs/AlInAs quantum *wire* superlattices [43–46] as shown in Fig. 2 (e) and (f), as well as an *fcc*-like $ABCABC\ldots$ stacking for IV–VI dot superlattices [38] as shown in Fig. 2(b). In the ideal case, these staggered stackings would correspond to a c-tetragonal or a trigonal *fcc*-like 3D dot lattice as illustrated schematically in Fig. 3 (a) and (b), respectively.

3. Interactions via elastic strain fields

The most important mechanism for multilayer correlation formation is based on the elastic strain fields of the buried dots. These strain fields are caused by the lattice-mismatch between the dots and the surrounding matrix material, which is the fundamental driving force for the Stranski–Krastanow growth transition. Due to this lattice-mismatch, each buried dot elastically deforms the surrounding matrix and generates a strain field that extends up to the spacer layer surface. During subsequent growth, these strain fields impose a bias on the diffusion current of deposited adatoms due to the corresponding gradient in the surface chemical potential. Therefore, a local enhancement of growth rate and thus, preferential island nucleation will occur at the strain minima on the wetting layer. In addition, preferential dot nucleation may also be enforced by the corresponding local reduction of the nucleation barriers for island formation.

The extended strain fields created by the buried dots depend on a large number of parameters such as their size and shape, their chemical composition, the thickness of the spacer layer, as well as the elastic properties of the materials and the crystallographic orientation of the growth surface. In order to understand and evaluate the possible stacking types, the details of these elastic strain fields must be taken into account. For this purpose, it is useful to consider two limiting cases: (i) the far-field limit, where the dot depth is large as compared to the dot dimensions; and (ii) the near-field limit, where the buried dots are very close to the growth surface. In the far-field limit, the internal structure as well as the actual size and shape of the dots can be neglected, i.e., the dots can be treated as simple point stress sources. This applies in a good approximation to the situation when the dot depth exceeds about two times the dot size [16,39]. In this situation, the surface strain distribution produced by each buried dot is determined solely by the elastic properties of the matrix (spacer) material and the crystallographic surface orientation. Therefore, the far-field limit is particularly instructive to reveal the general properties and the chemical trends of the elastic interlayer dot interactions.

For the simplest case of an elastically isotropic matrix material, the far-field stresses created by an individual buried dot can be derived analytically [58]. On the surface, one thus obtains a radially symmetric strain distribution $\varepsilon'_{\parallel}(r)$ given by

$$\varepsilon'_{\parallel}(r) = -\frac{P}{d^3} \cdot \left[\frac{2 - r^2/d^2}{(1 + r^2/d^2)^{5/2}}\right] \tag{1}$$

independent of the surface orientation. In this expression, d is the dot depth under the surface, $r = (x^2 + y^2)^{1/2}$ is the radial distance from the center above the dot, and P is the strength of the point stress source. The latter is given by $P = \varepsilon_0 V_0 (1 - \nu)/\pi$ [58], where ε_0 is the dot/matrix lattice-mismatch, V_0 is the dot volume and ν is the Poisson's ratio. On the wetting layer of the dot material formed on the spacer surface, the strain distribution is the sum of the homogeneous mismatch strain ε_0 and the inhomogeneous strain distribution $\varepsilon'_{\|}(x, y)$ created by the buried dot. Thus, the strain energy variation across the wetting layer surface $\Delta E_s(r) = E_s(r) - E_{s,0}$ can be written as:

$$\Delta E_s(r) = -(1 + \upsilon)\frac{E_{s,0} V_0}{\pi d^3} \cdot \left[\frac{2 - r^2/d^2}{(1 + r^2/d^2)^{5/2}}\right], \tag{2}$$

where $E_{s,0} = 2\mu(1 + \nu)\cdot\varepsilon_0^2/(1 - \nu)$ is the constant background strain energy due to the homogenous lattice-mismatch. Here, the higher order terms in $\varepsilon'_{\|}$ have been neglected because $\varepsilon'_{\|}(r) \ll \varepsilon_0$ in the far field limit, i.e., the strains due to buried point source are much smaller than ε_0. For the isotropic limit, evidently, $\Delta E_s(r)$ is also radially symmetric and its minimum resides directly above the buried dot with a value of $\Delta E_{s,\min} = -(1 + \nu)/\pi \cdot E_{s,0} V_0/d^3$. Also, the *shape* of the strain distribution is invariant when plotted as a function of the scaled surface coordinates r/d, which means that the width of the strain energy distribution scales as $1/d$. This is a general property of the far-field point source solution.

In contrast to the above assumptions, most materials of practical interest, in particular, most semiconductors exhibit a rather high degree of elastic anisotropy. As a result, the surface strain distribution produced by a buried stress source is significantly modified and shows a strong dependence on the surface orientation. To obtain the corresponding strain distributions, the equilibrium stress equations must be solved, taking the true elastic properties of the matrix as well as the boundary condition of a free surface with vanishing normal surface stresses into account. This can be done, e.g., using a Fourier method [40,59].

In cubic materials, the main elastic anisotropy axes are the ⟨100⟩ and ⟨111⟩ crystallographic directions, in which the Young's modulus E reaches its extremal values. Correspondingly, these directions represent either the elastically *hard* or *soft* directions. The degree of deviation from the isotropic case can be characterized by the dimensionless anisotropy ratio $A = 2c_{44}/(c_{11} - c_{12})$, which is essentially equal to the ratio E_{111}/E_{100} of the elastic moduli along the main anisotropy axes. For isotropic materials, E does not depend on the direction of the applied stresses and thus, $A = 1$. For anisotropic cubic materials, one has to consider two contrary cases, namely, that A is either larger or smaller than one. In the first case of $A > 1$, the ⟨111⟩ directions are the elastically hard directions and the ⟨001⟩ directions the soft directions ($E_{111}/E_{100} > 1$). This applies to all group IV, III–V and II–VI semiconductors with diamond or zinc-blende structure, in which the chemical bonds are along the ⟨111⟩ directions. The anisotropy is largest for the II–VI compounds, with $A = 2.04$ for ZnTe and 2.53 for ZnS. For the group IV semiconductors C, Si and Ge, A increases from 1.21, 1.56 to 1.64, respectively, and for the III–V compounds A ranges from 1.83 for GaAs to 2.08 for InAs. In the opposite case of $A < 1$, now ⟨100⟩ are the elastically hard directions and ⟨111⟩ the soft directions ($E_{111}/E_{100} < 1$). This applies, e.g., for materials with rock salt crystal structure in which the nearest neighbors are along the ⟨100⟩ directions. In particular, for the narrow gap IV–VI semiconductors with rock salt structure, the elastic anisotropy is particularly large, with $A = 0.18$, 0.27 and 0.51 for SnTe, PbTe and PbS, respectively.

With respect to the elastic strain fields, obviously, the most pronounced changes will occur for materials with large elastic anisotropy, i.e., when A strongly deviates from one. In this case, the strain distributions strongly depend on the surface orientation. Selecting two materials with large anisotropy but opposite directions of the anisotropy axes (PbTe, $A = 0.27$ and ZnSe, $A = 2.5$), the dependence of the normalized strain energy distributions on surface orientation is shown in Fig. 4 for a buried point-like island. It is evident that not only the strain energy distributions strongly differ from each other for the different surface orientations, but that they also show the opposite trend when A is either larger (ZnSe) or smaller than one (PbTe). As a general trend, it turns out that only when the surface is parallel to the elastically *hard* direction [(100) for ZnSe and (111) for PbTe] the strain energy minimum is exactly above the buried island, whereas in all other cases, the energy minima are laterally displaced. In particular, when the surface orientation is parallel to an elastically soft direction, the central minimum splits up into several energy minima, as is shown in panels (c) to (f) of Fig. 4.

In the far-field limit, the inclination directions where the surface minima are formed with respect to the buried dots are unique for each surface orientation and elastic anisotropy ratio. This is because the lateral displacements $r_{\min}$ of the energy minima scale linearly with the dot depth d. Thus, the corresponding characteristic inclination angle α between these directions and the surface normal $\vec{n}_s$ can be directly deduced according to $\alpha = \arctan(r_{\min}/d)$. Furthermore, the directions of the lateral displacements $\vec{q}_{\|,\min}$ of the energy minima within the growth plane are given by the projection of the elastically hard directions $\vec{\gamma}_{\text{hard}}$ that are closest to the surface normal onto the surface plane. Thus, $\vec{q}_{\|,\min} = (\vec{n}_s \times \vec{\gamma}_{\text{hard}}) \times \vec{n}_s$ where $\vec{\gamma}_{\text{hard}}$ is either a ⟨111⟩ or ⟨100⟩ direction, depending on if A is larger or smaller than one, respectively.

Fig. 4(k) shows the systematic variation of the interlayer correlation angle α as a function of the (*hkl*) surface orientation for three different materials with different elastic anisotropy (GaAs, ZnSe, and PbTe). In this plot, the (*hkl*) surface orientation is parameterized in terms of the angle β between (*hkl*) and the [100] direction (see Fig. 4(l)). Clearly, there is a systematic variation

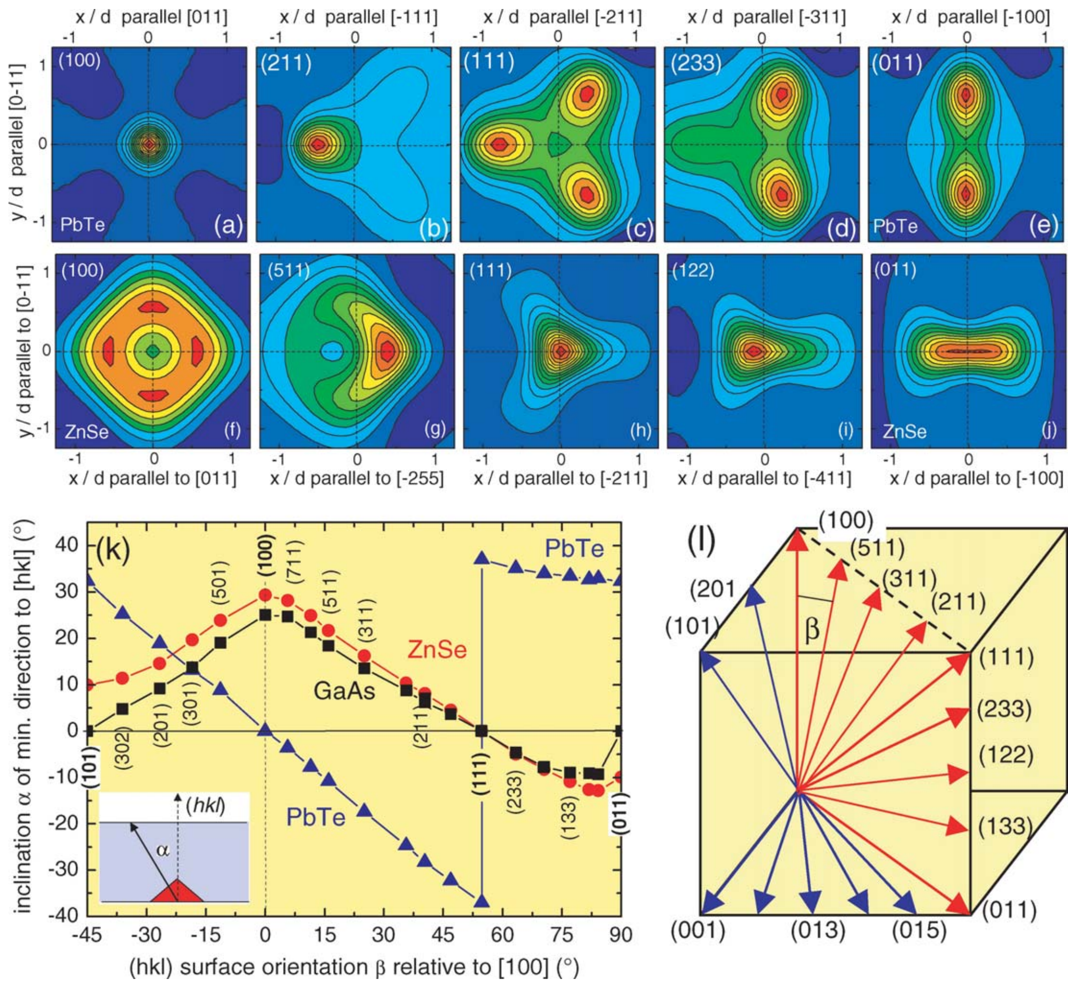

Fig. 4. Top: Surface strain energy distributions $\Delta E_s(x, y)$ above a point-like strained buried quantum dot for different surface orientations of PbTe (top row, $A = 0.28$) and ZnSe (second row, $A = 2.52$). The different orientations are indicated in (l). The energy distributions are shown as iso-energy contour plots as a function of reduced surface coordinates x/d and y/d, where d is the dot depth below the surface. The red color indicates areas of lower strain energy. Clearly, for most surface orientations the strain energy minima are displaced from the center, and when the surface normal is parallel to an elastically soft direction, a splitting into several *side minima* occurs. The dependence of the inclination angle α at which the energy minima appear on the surface relative to the (*hkl*) surface normal is plotted in (k) as a function of the angle β between the (*hkl*) and the (100) plane.

of α as the surface orientation is tilted from (100) through (111) and (011). In particular, the largest interlayer correlation angles appear when the surface is parallel to the elastically soft direction [i.e., (100) for $A > 1$ and (111) for $A < 1$], whereas the minima are almost vertically aligned when the surface is close to the elastically hard direction. In addition, it is again evident that the behavior of materials with $A > 1$ is opposite to those with $A < 1$.

If we now compare the different materials with the same hard axis (ZnSe and GaAs in Fig. 4(k)), one can see that the larger the elastic anisotropy ($A_{\mathrm{ZnSe}} > A_{\mathrm{GaAs}}$), the larger the lateral minima displacements. A systematic analysis of this trend shows that the lateral minima displacements and thus, the correlation angles α depend in a linear way on the anisotropy ratio [40]. For the most relevant high symmetry (100) and (111) directions, a splitting of the energy minima occurs if the anisotropy exceeds the critical value of $A_c > 1.4$ for (100) and $A_c < 0.6$ for (111). Beyond these values α varies linearly according to $\alpha_{100} = 56^\circ \times (1 - 1.1 \times A^{-1})$ for (100) and $\alpha_{111} = 50^\circ \times (1 - A)$ for (111) [40]. Thus, α_{100} increases from 16°, to 23° and 32° for Si, GaAs and ZnSe, respectively, and α_{111} from 19°, to 36° and 41° for PbS, PbTe and SnTe. A similar behavior can be expected also for all other surface orientations.

4. Comparison with experimental results

For quantum dot multilayers with large spacer thickness and large lateral dot spacings there is little overlap of the strain fields of neighboring buried dots. Thus, the far-field model can be directly applied to predict the interlayer dot correlations – provided that the energy minima are deep enough to enforce a correlated nucleation process. The dots should then replicate in the directions of the strain energy minima on the surface created by the buried dots (Fig. 4). Thus, *inclined* interlayer dot correlations are expected for almost all growth orientations with interlayer correlation angles corresponding to those plotted in Fig. 4(k). Moreover, for surface orientations where several laterally displaced surface energy minima appear, staggered types of dot stackings should be formed provided that the splitting of the minima is sufficiently large.

Experimentally, up to now, interlayer correlations in multilayer structures have been studied in detail only for the main (100) and (111) growth orientations. For (001) growth and elastic anisotropy A larger than 1.5, four side energy minima are formed by the strain fields of each buried point dot (Fig. 4(f)). These minima define a preferred square dot arrangement within the subsequent growth plane and an $ABAB\ldots$ vertical stacking sequence as shown schematically in Fig. 3(a). In the ideal case, this then yields an overall body-centered tetragonal 3D dot arrangement in which the dots are laterally placed in a square lattice along the $\langle 100\rangle$ directions. For the (111) growth orientation and A smaller than 0.6, the three side minima in the energy distributions (Fig. 4(c)) create a triangle with equally long sides. This defines a preferred 2D hexagonal lateral ordering of the dots along the $\langle 2\bar{1}\bar{1}\rangle$ surface directions as well as an *fcc*-like $ABCABC\ldots$ interlayer dot stacking. This is shown schematically in Fig. 3(b), and corresponds to an overall 3D trigonal dot lattice. Since, practically, the first quantum dot layer in a multilayer stack is just as disordered as a single dot layer, the transition to the ordered structures in the multilayers induced by the dot interactions will be always not abrupt but rather gradual. This has been demonstrated, e.g., in detail in [25] for PbSe dot superlattices. In addition, it may turn out that the dot size and density as defined by a given set of growth conditions is not compatible with the expected stacking type and ordered lateral dot arrangement [39,42]. Thus, only for a certain set of growth parameters this ordering transition will actually occur.

Concerning the investigated material systems, most extensive studies have been performed for the prototype Si/Ge (100), InAs/GaAs (100) and PbSe/PbEuTe (111) multilayer systems, for which in principle, staggered dot stackings are expected in the far-field limit. For PbSe dot multilayers, indeed a very well ordered *fcc*-like $ABCABC\ldots$ dot stacking has been observed for PbEuTe spacer thicknesses d larger than 40 nm, as demonstrated clearly by the cross-sectional TEM image shown in Fig. 2(b). In addition, the experimentally deduced interlayer dot correlation angle of $\alpha = 39^\circ$ [16,38] agrees very well with the theoretical angle of $\alpha = 36^\circ$ predicted by the far-field model (Fig. 4(k)), and the measured lateral dot spacing within in the growth plane scales linearly with PbEuTe spacer thickness [16,38]. Thus, self-organized *fcc*-like 3D lattices of dots can be obtained with tunable lattice constant [16]. A further analysis shows that in this case, the lateral dot spacing is essentially equal to the energy minima separation of $L_{\min} = \sqrt{3}\, d \tan\alpha_{111}$ calculated from the far-field model. Also, the in-plane hexagonal lateral ordering of the dots as expected from the triangular energy minima arrangement of Fig. 4(c) is clearly reproduced in the experiments [16,25]. This is evidenced by the plan-view TEM image depicted as inset in Fig. 2(b). On the other hand, when the dot layer separation is decreased to below 40 nm, experimentally, a transition from the *fcc*-type stacking to a vertical dot alignment is observed [38,39,42]. As will be discussed in detail in the next section, this is due to the finite size of the dots and the characteristic changes in the strain fields in the near-field limit.

The situation is quite different for the Ge/Si and InAs/GaAs (100) cases. There, the minima separation $L_{\min}$ in the strain energy distributions is much smaller as compared to that for the PbSe/PbEuTe (111) case. This is due, on the one hand, to the fact that the elastic anisotropy and thus, the correlation angles of $\alpha = 16^\circ$ and 23° for Si and GaAs are much smaller than that for the PbSe/PbEuTe case (see Fig. 4(k)) and that, on the other hand, *four* instead of *three* side energy minima are formed. Accordingly, even for spacer thicknesses d as large as 50 nm the energy minima separation $L_{\min} = \sqrt{2}\, d \tan\alpha_{100}$ is still only 20 or 34 nm for Si/Ge or InAs/GaAs, respectively, as compared to 62 nm for the PbEuTe (111) case. Because this is less than the typical lateral island sizes observed in these material systems, it is not possible for the surface islands to occupy just one single energy minimum. Thus, up to now an $ABAB\ldots$ stacking like the one shown in Fig. 3 (b) has not been observed in these systems, but only a vertical dot alignment, as exemplified in Fig. 2(a) for an InAs/GaAs superlattice. This indicates that for Si/Ge as well as III–V multilayer systems, the elastic anisotropy may not be sufficiently large to obtain a staggered dot stacking for the useful range of growth conditions.

For the II–VI semiconductors, the elastic anisotropy is significantly larger as compared to that of the III–V compounds. Thus, there is a stronger tendency for the formation of a staggered dot stacking and indeed, 'anticorrelated' interlayer stackings have been found for CdSe/ZnSe [35,36] as well as CdTe/ZnTe [37] multilayers. This is illustrated by the cross-sectional TEM image of a CdTe/ZnTe multilayer shown in Fig. 2(e), exhibiting vertically anticorrelated ZnTe islands [37]. This is obviously similar to the theoretically expected $ABAB\ldots$ stacking shown in Fig. 3 and results from the fact that a local energy *maximum* is formed directly above each buried dot. Therefore, this point is not favorable for subsequent island nucleation. On the other hand, because the four side minima in the surface strain energy distributions are separated only by a weak saddle point (see Fig. 4(f)), there is no strong lateral ordering tendency for the subsequent surface islands. Therefore, the dots remain rather

disordered in the lateral direction and are thus only 'anticorrelated' along the growth direction. In addition, the experimentally derived interlayer correlation angles [35–37] are significantly larger than those expected from the point source calculations (e.g., $\alpha = 40^\circ$ in the TEM image of Fig. 2(e) as compared to $\alpha = 28^\circ$ from Fig. 4(k)). This may result from the overlap of the strain fields of neighboring buried dots, which obviously modifies the overall surface strain distribution, but also other mechanism could contribute to the interlayer correlation formation in these materials (see Secion 6).

The effect of overlapping strain fields has been modeled by Shchukin et al. [41] by considering the elastic interaction energy between sheets of periodic square 2D arrays of strained nano-islands using a Green's function approach. By calculating the interaction energy as a function of the relative vertical and lateral displacements of the 2D island arrays it was found that for certain spacer thicknesses, the interlayer interaction energy is indeed minimized when the islands are *anticorrelated* in successive layers. For II–VI superlattices, thus, a transition from a vertical dot alignment to an anticorrelation was predicted when the spacer thickness exceeds more than three times the lateral array period. This agrees roughly with the experimental observations [36,37]. As shown in Section 5, also the single dot strain model predicts a transition between vertically aligned and staggered dot stacking in the near-field limit. In any case, it is emphasized that the high elastic anisotropy of the II–VI materials is the crucial factor that gives rise to the vertical anticorrelation. The drawback of the model of Shchukin et al. [41] is that it does not yield any predictions on the lateral dot ordering process and the preferred lateral dot spacing. This is because a perfectly ordered lateral dot array has to be assumed as a starting point of these calculations.

Anticorrelated stackings have also been observed for self-organised InAs/AlInAs quantum wire superlattices on InP (001) [43–45,60,61], which is shown in Fig. 2(d). Although this anticorrelation again complies with the basic trend deduced from the anisotropic strain field model, also in this case, the observed interlayer correlation angles of around 40° are significantly larger than predicted by the point source model. Therefore, additional interlayer interaction mechanisms based on compositional modulations of the alloy spacer layer have been invoked as origin for these anticorrelated stackings [45,46]. This will be discussed in detail in Section 6. A particularly interesting mixed-type stacking has been also found recently for two-fold stacked InAs quantum dots grown on 2D periodically patterned (001) GaAs substrate templates [62]. In this case, two different dot types nucleate in the second layer, one in the on top positions and the other one in the staggered positions. This special stacking again could be explained only when taking the elastic anisotropy of the materials into account [62].

Apart from the modeling of the dot stackings, the point source model can be also used to address the question of the magnitude of the interaction energies required for the formation of interlayer dot correlations. Comparing a large number of experimental results, interestingly it turns out that for various different material systems and superlattice structures, interlayer dot correlations are found to persist to interlayer spacings of about up to 40 to 60 nm [13,28,34,38]. Since for large spacer layer thicknesses the point-source approximation holds, one can readily calculate the corresponding depth of the energy minima $\Delta E_{\mathrm{s,min}}$ produced by each buried quantum dot island using

$$\Delta E_{\mathrm{s,min}} = -C^*_{\mathrm{hkl}} \cdot E_{\mathrm{s,0}} V_0 / d^3. \tag{3}$$

In this relation, C^*_{hkl} is a constant derived from the numerical strain calculations that only depends on the elastic constants and the (*hkl*) surface orientation, and $E_{\mathrm{s,0}}$ is the constant strain energy density in the unperturbed 2D wetting layer caused by the layer/substrate lattice-mismatch. These are characteristic for a given material system and growth orientation. From the above far-field calculations, C^*_{100} is obtained as ≈ 0.52 for Si and GaAs (100) and $C^*_{111} \approx 0.69$ for PbEuTe (111). In addition, for InAs/GaAs, Si/Ge and PbSe/PbEuTe, the homogenous misfit strain energy $E_{\mathrm{s,0}}$ is of the same order of magnitude of around 100 meV/atom pair, as indicated in Table 1.

In order to estimate the volume of the buried nano-islands, we utilize the fact that for a given material system, the nano-islands usually exhibit a pyramidal shape with well-defined side facets. For Ge these can be either {105} facet for the hut cluster islands [63] (which we consider here), or multiple higher indexed facets for the larger dome-shaped islands [64–66]. For InAs islands, several different facets have been reported [67], but for the sake of simplicity we approximate them by {113} facets. For PbSe islands only {100}-type facets have been observed [68]. Using the typical dot base widths of 60 nm for Ge

Table 1

Characteristic experimental parameters for island sizes and shapes used for calculation of the minimal strain energy minima ΔE_{crit} per atom pair required for the formation of interlayer correlations in self-assembled quantum dot superlattices (Eq. (3)), using a cut-off for the interlayer correlations at a critical interlayer spacing of $d_{\mathrm{crit}} = 50$ nm as a typical experimental value for different material systems. ε_0 is the dot/matrix mismatch strain, b_{typ} is the typical island base width, V_{typ} is the resulting typical island volume, C^*_{hkl} is the constant used in Eq. (3) for calculating the depth of the energy minima and $E_{\mathrm{s,0}}$ is the strain energy for the homogenous pseudomorphic 2D layer case

Multilayer system	Growth orientation	ε_0 (%)	b_{typ} (nm)	Island facets	V_{typ} (nm^3)	C^*_{hkl}	$E_{\mathrm{s,0}}$ (meV)	ΔE_{crit} (meV)
Ge/Si	(100)	4.0	60	(501)	7200	0.52	77	2.2
InAs/GaAs	(100)	6.9	30	(311)	4270	0.52	128	2.2
PbSe/PbEuTe	(111)	5.2	30	(100)	1600	0.69	142	1.2

and 30 nm for InAs and PbSe islands, one can then calculate the corresponding volume of the islands V_{typ} as listed in Table 1. If we further assume that, in spite of the frequently observed shape changes of the buried islands, their effective volume is preserved during overgrowth, then for the experimentally observed cut-off interlayer spacing of $d_{crit} = 50$ nm, a minimal depth of the strain energy minima $\Delta E_{s,min}$ of the order of only 1–2 meV per atom pair is consistently derived for these material systems that is required in order to induce interlayer correlations in the multilayer structures. This is shown in detail in Table 1. Although, the actual island sizes and critical spacer thicknesses will obviously vary according to the chosen growth conditions, it is evident that the magnitude of these energies is not only more than a factor of 20 smaller than the strain energies $E_{s,0}$ of the homogeneous 2D wetting layers, but also one order of magnitude lower than the typical thermal energies $k_B T$ during growth. Up to now, it has not yet been resolved how such small interaction energies give rise to the interlayer correlations and how exactly they influence the dot nucleation process.

5. Finite size effects for elastic interactions

For quantum dot multilayers with small spacer layer thickness, obviously the actual size and shape of the buried dots can no longer be neglected. Thus, the far-field limit does not hold and the strain distributions must be evaluated separately for each particular situation. As a general trend, when the buried dots are close to the surface the strain fields are focused more strongly in the vertical growth direction such that the surface energy minima are confined closely to the center above the dots. As a consequence, for small spacer thicknesses the dots generally tend to be aligned along the growth direction.

For the PbSe/PbEuTe (111) case, detailed studies on the dependence of the stacking as a function of spacer layer thickness have been performed [38,39]. In particular, at a spacer layer thickness below about 40 nm, a transition from the *fcc*-like $ABCABC\ldots$ stacking to a vertical dot alignment was observed, for spacer layer thicknesses exceeding 56 nm only uncorrelated superlattices were found [38]. This is exemplified in Fig. 5 by whereas representative cross-sectional TEM images of three different PbSe quantum dot superlattices with different PbEuTe spacer layer thickness of $d = 32$, 47 and 68 nm from (g) to (i), respectively. The same type of transitions were also found when the PbSe dot size was varied from 6 to 20 nm by changing the growth temperature [42] or by changing the PbSe dot layer thickness [39]. Similar changes in the interlayer correlations were also found for other material systems [36].

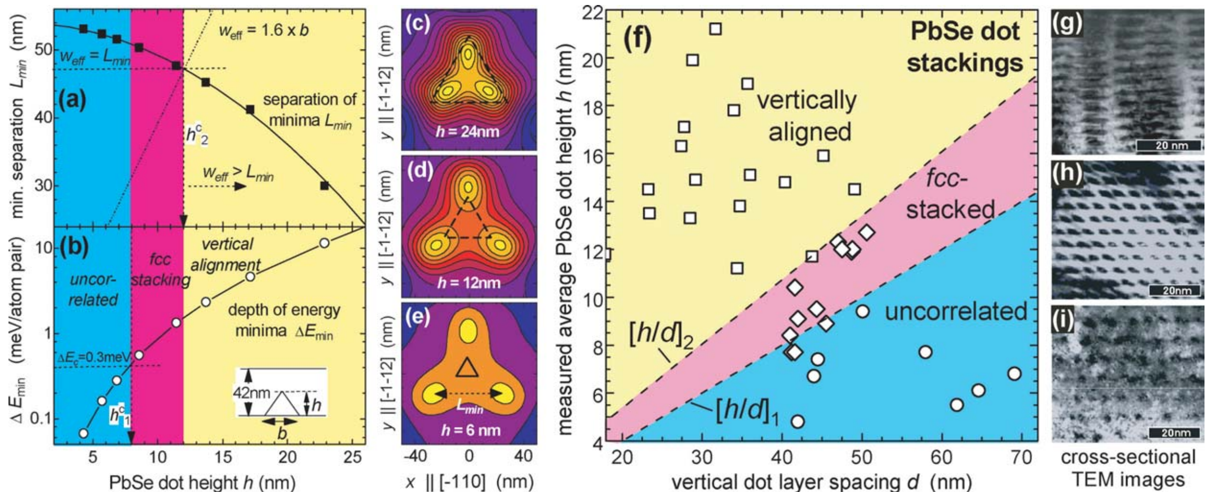

Fig. 5. Left-hand side: Influence of the actual dot size on the strain energy distributions and interlayer correlations in (111) PbSe/PbEuTe quantum dot superlattices. (a) The dependence of the energy minima separation L_{min} (■) and (b) the dependence of the minima depth ΔE_{min} (○) as a function of dot height for a constant dot depth of $d = 42$ nm below the surface. Examples of the corresponding surface strain energy distributions are shown in (c) to (e) for dot heights of $h = 24$, 12 and 6 nm with iso-energy line spacings of 0.65, 0.13, and 0.046 meV/atom pair, respectively. The dot bases corresponding to the different dot sizes are indicated by the dashed triangles in the energy contour plots. The dashed-dotted straight line in (a) indicates the dependence of the effective dot base width $w_{eff} = 1.6 \cdot b$ required by each dot and the red area indicates the parameter range for which an *fcc* dot stacking is expected from the calculations. Right-hand side: (f) Phase diagram of different dot stackings in PbSe dot superlattices as a function of vertical dot layer spacing and PbSe dot size as obtained from x-ray diffraction, TEM and AFM measurements: vertically aligned (□), *fcc*-stacked (◇) and uncorrelated superlattices (○). The dashed lines indicate the phase boundary conditions given by Eqs. (4) and (5). Examples of the corresponding TEM images for each stacking case are shown on the right-hand side for dot layer spacings of $d = 68$, 46 and 32 nm from (g) to (i), respectively.

In order to explain these transitions, the changes in the surface strain energy distributions as a function of depth and size of the buried dots must be evaluated. According to AFM studies [68], PbSe surface dots exhibit a pyramidal shape with triangular base defined by $\{100\}$ side facets, thus having a fixed aspect ratio of $a = b/h = \sqrt{6}$. Assuming an identical shape for the buried dots, the surface strain distribution for a given dot depth and dot size can be obtained by a convolution of the point source stress solution over the island shape. Fig. 5 (c)–(e) shows three examples of such calculated surface strain energy distributions $\Delta E_S(x, y)$ for PbSe dots at a constant depth of 42 nm but with different dot height of $h = 6$, 12 and 24 nm, respectively. Although in all three cases, $\Delta E_S(x, y)$ exhibit three side minima, the separation $L_{\min}$ of these minima continuously decreases with increasing dot size, whereas the minima depth $\Delta E_{\min}$ rapidly increases. This is shown in Fig. 5 (a) and (b), respectively.

To determine which type of interlayer correlation will be actually formed during growth, one has to compare the minima separation $L_{\min}$ with the dot base width b as is indicated by the dashed triangles in Fig. 5 (c)–(e). For small dots, the minima separation is much larger than the dot base width. Therefore, each dot on the surface can easily occupy just one single energy minimum. As superlattice growth proceeds, therefore, an *fcc*-like *ABCABC*... stacking sequence is formed. For very *small* dots, however, the energy minima are very shallow, because their depth decreases linearly with decreasing dot volume (see Eq. (3)). According to experimental results, however, a minima depth of more than ~ 0.3 meV/atom pair is required for correlated dot nucleation [38]. This corresponds to a total minimum depth of ~ 1 meV/atom pair because for the *fcc* stacking each surface minimum is created by the overlap of the minima of three neighboring subsurface dots. As indicated by the horizontal dashed line in Fig. 5(b), thus, no interlayer dot correlations should be formed when the dot heights are below the critical value of $h_1^c = 8$ nm for $d = 42$ nm. As shown in [39], this is in good agreement with experimental observations.

For large dots the energy minima separation successively *decreases* as indicated in Fig. 5(a) and eventually they are merged to one single minimum when d is less than two times of the dot base width [38]. Obviously, a vertical dot alignment will result under these conditions. To determine the exact point where this transition occurs, one has to compare the minimal lateral space w_{eff} required for the growth of a single dot with the surface strain energy minima separation. Experimentally, it turns out that this minimal dot separation is actually about 1.6 times larger than the mere dot base width. This may be attributed both to the existence of a denuded zone around each dot in which further dot nucleation is suppressed, as well as to repulsive elastic lateral island interactions. Applying this condition to the data shown in Fig. 5(a), a critical dot size of $h_2^c = 12$ nm is deduced (dashed dotted line) above which w_{eff} is smaller than $L_{\min}$ and where thus, a transition from fcc-stacking to a vertical dot alignment should occur. This is again in good agreement with our experimental observations [39,42].

For a given material system, these phase boundary conditions can be written in a rather generalized form under the condition of an invariant island shape. The cut-off length of the interlayer correlations is given by a minimal interaction energy E_{crit} required for correlated dot nucleation that is specific for each material system and growth condition. According to Eq. (3), this energy is determined only by the volume over the dot depth ratio. As for a fixed island shape, V_0 is proportional to h^3, this cut-off condition can be reformulated as:

$$[h/d]_1 = \sqrt[3]{\frac{E_{\text{crit}}}{E_0 C^*_{\text{hkl}} \delta}}, \tag{4}$$

where $\delta = V_0/h^3$ is constant for a given island shape. Using for PbSe the values $E_{\text{crit}} = 3 \times 0.3$ meV, $\delta = \sqrt{3}/2$ and the parameters listed in Table 1, one obtains a critical ratio of $[h/d]_1 = 0.22$ below which no interlayer correlations should be formed in PbSe/PbEuTe superlattices.

Likewise, because for a fixed island shape $w_{\text{eff}} \sim h$ and the minima correlation angle α is constant for a given h/d ratio [40], the condition of $w_{\text{eff}} = L_{\min}$ for the transition between the vertical dot alignment and *fcc* stacking can be written for the (111) case as:

$$[h/d]_2 = \frac{\sqrt{3} \cdot \tan \alpha_{111}}{\kappa \cdot a}, \tag{5}$$

where a is the aspect ratio of the islands and $\kappa = w_{\text{eff}}/b$ is the constant characterizing the exclusion zone of the island. For the (100) growth orientation, the $\sqrt{3}$ factor simply has to be replaced by $\sqrt{2}$ because of the different arrangement of the energy minima. Applying the appropriate parameters for the PbSe case ($\kappa = 1.6$ and $a = \sqrt{6}$), one obtains a critical ratio of $[h/d]_2 = 0.28$ above which all PbSe dots should be vertically aligned. Thus, only in the range of $0.22 < [h/d] < 0.28$ an *fcc*-like dot stacking should occur.

Compiling in Fig. 5(f) our whole body of experimental data obtained by X-ray diffraction, TEM and AFM for more than 50 different PbSe quantum dot superlattices with different spacer thicknesses and dot sizes, a clear phase diagram of dot stackings is obtained in which the phase boundaries indeed follow exactly the boundary lines defined by the stacking conditions. This phase diagram demonstrates that generally a staggered stacking of dots can be obtained only in a narrow window of conditions confined by the phase boundaries of Eqs. (4) and (5). Its width is determined not only by the island shapes, the elastic material properties and the growth orientation, but also depends on the conditions used for epitaxial growth. In fact, it may be very

narrow or even absent (i.e., $[h/d]_2 < [h/d]_1$) for a given material system. This puts a strong limitation on the growth conditions and material combinations in which a staggered dot stackings can be obtained.

6. Other interaction mechanisms

Elastic interactions are certainly the most important mechanism for the formation of interlayer correlations in strained quantum dot multilayers. However, as already indicated in Fig. 1, there exist at least two other alternative but less obvious mechanisms that may contribute to interlayer correlation formation. These are the correlated dot nucleation mediated by (i) a non-planarized surface topography (Fig. 1 (c) and (d)), or by (ii) a lateral compositional modulation within the spacer layer (see Fig. 1 (e) and (f)). Although up to now, little work has been performed to address these mechanisms, each of them in principle may also give rise to different interlayer dot stacking types, depending on the intricate details of the interaction and nucleation process (see Fig. 1).

With respect to the correlations mediated by the growth morphology, one first has to realize that each quantum dot layer represents a highly corrugated surface topography. Although during overgrowth, this 3D surface tends to planarize in order to minimize the surface energy, a corrugated nonplanar surface structure is retained when the capping process is incomplete or is hindered by sluggish planarization kinetics. Obviously, the existence of a corrugated surface will influence subsequent island nucleation and, because the surface corrugations are linked to the buried dots, interlayer dot correlations will then be produced as well. The profound role that surface morphology plays in the dot nucleation process has been recently underlined by the investigations of self-assembled quantum dot growth on prepatterned substrates, where it was found that dot nucleation can be triggered by lithographically defined surface sites [69,70]. In fact, by this means, a near-perfect position control of self-assembled quantum dots has been achieved, as demonstrated for Ge/Si [69] as well as for InAs on GaAs dots [70].

Considering the overgrowth of Stranski–Krastanow islands, actually two different types of surface morphologies may be formed. On the one hand, when the surface diffusivity of the spacer adatoms as well as surface capillarity forces are small, surface planarization is rather slow and thus, mound-like structures are retained above the buried islands when the spacer layer thickness is not very large. This situation is illustrated schematically in Fig. 1 (c) and (d). On the other hand, when surface mass transport is dominated by the stress fields of the buried dots, the mobile surface adatoms during spacer layer growth are repelled from the surface area above the buried dots [13] due to the opposite sign of the mismatch strain. As a result, the growth of the spacer layer is locally suppressed and thus, surface depressions or pits are formed above the buried dots [13]. This has been observed, e.g., for InAs islands overgrown by GaAs [71] or InP [72]. This means that in essence, the actual type of surface morphology formed during overgrowth strongly depends on the chosen growth conditions.

A second complication arises from the fact that the reaction of dot nucleation to the presence of a non-planar corrugated surface morphology itself depends on the dominating mechanism of surface mass transport. If surface mass transport during wetting layer growth is dominated by capillary forces, then dot material will accumulate at the concave surface areas. As a result, preferred dot nucleation will occur at the troughs of the surface morphology. This is illustrated in panel (d) of Fig. 1. Experimentally, this behavior has been observed for example for Ge growth on patterned Si, where Ge islands were found to nucleate preferentially at the bottom of nano holes etched into the Si substrate [69,73], and a similar behavior was also found for InAs islands grown over GaAs hole patterns [70]. On the other hand, when surface mass transport is dominated by stress-driven surface diffusion, the opposite behavior will occur because the adatoms then diffuse preferentially towards the convex parts of the surface morphology where part of the misfit strain is elastically relaxed. As a result, the deposited dot material will diffuse to the tops or edges of the surface mounds where consequently, subsequent dot nucleation will occur. This type of behavior has been observed, e.g., for InAs quantum dots deposited on GaAs surface ridges or mesas [74–76], as well as for Ge grown over Si mesas [77,78]. Both effects can be further altered when there exist large differences in the free surface energies or diffusivities on the differently oriented portions of the surface morphology. In the light of these complexities, the existence of a non-planar spacer layer surface can give rise to a vertical alignment when the dots nucleate preferentially on the mounds above the buried islands, or a staggered stacking when dot nucleation occurs in the troughs in between.

An example for the profound effect of the spacer morphology on the interlayer dot correlation is shown in Fig. 2(c) for a Ge/Si dot superlattice [55]. In this case, as a result of the increasing Ge dot size in the superlattice stack, no complete planarization of the thin Si spacer layers is achieved and, as a result, the dot alignment switches to an oblique replication at a certain point of superlattice growth [55]. Other examples for non-vertical stackings possibly related to non-planarized spacer layer morphologies include self-assembled InP/GaInP quantum dot stacks [79] as well as InAs/InP [80] and InAs/InAlAs [45, 81] quantum wire multilayers, in which oblique interlayer dot alignments with varying correlation angles as well as staggered wire stackings have been observed by TEM (see Fig. 2(d)).

The final mechanism for interlayer correlation formation is based on lateral variations in the chemical composition of the spacer layer induced by the buried dots. As is indicated in Fig. 1 (e) and (f), these variations may originate from two different processes, namely, from preferential surface segregation of dot material above the buried islands (Fig. 1(e)), or secondly, from

strain or morphology induced alloy decomposition of the spacer layer (see Fig. 1(f)). The first mechanism will be operative for strongly segregating heteroepitaxial systems. This applies for many of the self-assembled quantum dot material systems because they are composed of materials with large differences in lattice-constants and binding energies, which are two of the major driving forces for surface segregation. As surface segregation will tend to cause an enhanced accumulation of dot material on the surface directly above the buried dots, during subsequent dot layer deposition, the wetting layer growth is locally enhanced and thus, the dots will nucleate preferentially on top of the buried dots. Practically, this effect is superimposed by the simultaneous action of the elastic strain fields of the buried dots that for thin spacer layers tends to produce a vertical dot alignment as well. Therefore, up to now there exist no clear experimental evidence on how much surface segregation actually contributes to interlayer correlations in multilayer structures. Never the less, several studies have indicated that in multilayers the critical wetting layer for island nucleation is successively reduced with increasing number of deposited layers [52–54]. This may be taken as an indication that surface segregation is an important factor in multilayer growth. Surface segregation strongly depends on the growth conditions and can be strongly altered by the use of surfactants [82]. This may provide a tool for studying and controlling its effect in multilayer structures.

For multilayers with multi-component alloys as spacer layers, lateral compositional variations can be also caused by the tendency of some alloys to decompose into regions of different chemical composition, driven by strain or surface corrugations during epitaxial growth. Alloy phase separation is quite common in III–V ternary or quaternary alloys for certain chemical compositions and growth conditions (see, e.g., [83] for a review). The resulting lateral variation of the chemical composition in the spacer layer may not only cause a chemical composition modulation as well, but will also induce a lateral variation in the strain due to the variations in the spacer layer lattice constant. This may amplify or counteract the strain fields arising from the buried dots, but in any case, both effects will lead to a nonuniform dot nucleation on the spacer layer surface and to the formation of interlayer dot correlations.

The most prominent example for this mechanism are the staggered stackings observed in self-assembled InAs/AlInAs (001) quantum wire superlattices [43–46,60,61], as exemplified by the TEM image shown in Fig. 2(d). In this case, the ternary AlInAs spacer layers show a strong tendency of alloy decomposition due to the immiscibility gap [45,84]. Under the presence of surface roughness or strain variations during growth, lateral phase separation in In-rich and Al-rich regions occurs [84–86], and as a result, In-rich V-shaped regions are formed in the AlInAs spacer layers, emerging from the side faces of the buried InAs quantum wires. This is revealed by the chemical contrast in cross-sectional TEM images as indicated by the dashed arrows in Fig. 2(d) (see [45,46] for more details). Subsequently, InAs quantum wires nucleate preferentially at the intersections of In-rich V arms of neighboring buried wires, which gives rise to a staggered *ABAB*... interlayer stacking that is clearly visible in Fig. 2(d). This stacking type has been observed consistently by several groups for varying AlInAs spacer layer thicknesses from 2.5 to 30 nm [46,60] with corresponding interlayer correlations angles of around 40°. Apart from the chemical contrast visible in the TEM image [45,46], strong supporting evidence for this mechanism comes from the fact that no such staggered stacking was found when the AlInAs spacer layers were replaced by GaInAs or GaInP spacers, for which the usual vertical alignment was found [44,56,61]. This clearly underlines that this staggered correlation is based on chemical effects, which has been successfully explained by a model developed by Priester and Grenet [47]. On the other hand, in the TEM images it seems that due to the slow surface kinetics, AlInAs spacer layers are not always completely planarized prior to subsequent InAs growth. Therefore, the surface morphology could also play a significant role in the formation of the staggered correlations in these material systems. In fact, in Ref. [80], an inclined alignment of InAs quantum wires was reported also for pure InP spacer layers in which alloy decomposition does not exist.

7. Summary and conclusions

In summary, different interlayer stackings can be formed in self-assembled quantum dot multilayers based on different mechanisms. These are (i) elastic interactions mediated by the buried dot strain fields; (ii) morphological interactions due to nonplanarized spacer topographies; or (iii) by interactions based on chemical composition variations within the spacer material. All three mechanisms can give rise to a vertical dot alignment as well as to staggered dot stackings, depending on the details of the interaction process and growth parameters. Thus, even for a single material system, the interlayer correlations may change from one stacking type to another as a function of spacer layer thickness, dot size or growth conditions. The stackings have a profound effect on the lateral ordering of the dots within the growth plane, which is of importance because this is a key prerequisite to achieve a narrowing of the size distribution as is required for device applications. Although not treated here in detail, staggered dot stackings are particularly effective for inducing a lateral dot ordering process [16,25,43,45] due to the fact that in this case, the dot nucleation sites are determined by the interactions with several neighboring dots below the surface, whereas for vertically aligned dots, the initial lateral arrangement is mainly replicated from layer to layer along the growth direction with only a weak lateral ordering tendency [51,87,88]. This different behavior has also been found in Monte Carlo superlattice growth simulations [40].

While the stackings due to elastic interactions are now quite well understood, there are still ample open issues to be resolved for the other interaction mechanisms. This is due to their strong dependence on the specific growth conditions, but also due to the fact that they are always superimposed by the simultaneous action of the strain field interactions. Therefore, much further work is still needed to clarify their role in multilayer dot structures. On the other hand, the interplay between the different mechanisms may be utilized to create new and more complex interlayer stacking types and thus novel quantum dot superstructures. This may be achieved, e.g., by alternating material combinations, spacer thicknesses as well as growth conditions during growth, or by combining compressively and tensily strained dot structures, as well as by combining interlayer stacking with pre-patterning of substrate templates. The latter will allow to tailor the initial dot arrangement and thus may ultimately lead to the synthesis of fully controlled three-dimensional nanostructures.

Acknowledgements

The author would like to thank V. Holy for the strain field calculations, as well as M. Pinczolits, A. Raab, R. Lechner, J. Stangl, L. Salamanca-Riba, H.H. Kang and G. Bauer for their contributions to the experimental results. This work was supported by the FWF and GME of Austria.

References

[1] D. Bimberg, M. Grundmann, N.N. Ledentsov, Quantum Dot Heterostructures, Wiley, Chichester, 1998.
[2] D. Leonard, M. Krishnamurty, C.M. Reaves, S.P. Denbaar, P. Petroff, Appl. Phys. Lett. 63 (1993) 3203.
[3] J.M. Moison, F. Houzay, F. Barthe, L. Leprince, E. Andre, O. Vatel, Appl. Phys. Lett. 64 (1994) 196.
[4] V.A. Schchukin, N.N. Ledentsov, D. Bimberg, Epitaxy of Nanostructures, Springer-Verlag, Berlin, 2004.
[5] D.J. Srolovitz, Acta Metall. 37 (1989) 621.
[6] C.W. Snyder, B.G. Orr, D. Kessler, L.M. Sander, Phys. Rev. Lett. 66 (1991) 3032.
[7] D.J. Eaglesham, M. Cerullo, Phys. Rev. Lett. 64 (1990) 1943.
[8] H. Gao, J. Mech. Solids 39 (1991) 443.
[9] C. Ratsch, A. Zangwill, Surf. Sci. 293 (1993) 123.
[10] J. Tersoff, F.K. LeGoues, Phys. Rev. Lett. 72 (1994) 3570.
[11] I. Daruka, A.-L. Barabási, Phys. Rev. Lett. 79 (1997) 3708.
[12] J.Y. Marzin, J.M. Gerard, A. Izrael, D. Barrier, G. Bastard, Phys. Rev. Lett. 73 (1994) 716;
R. Leon, P.M. Petroff, D. Leonhard, S. Fafard, Science 267 (1995) 1966.
[13] Q. Xie, A. Madhukar, P. Chen, N. Kobayashi, Phys. Rev. Lett. 75 (1995) 2542.
[14] G.S. Solomon, J.A. Trezza, A.F. Marshall, J.S. Harris Jr., Phys. Rev. Lett. 76 (1996) 952.
[15] C. Teichert, L.J. Peticolas, J.C. Bean, J. Tersoff, M.G. Lagally, Phys. Rev. B 53 (1996) 16334.
[16] G. Springholz, V. Holy, M. Pinczolits, G. Bauer, Science 282 (1998) 734.
[17] L. Vescan, W. Jäger, C. Dieker, K. Schmidt, A. Hartmann, H. Lüth, Mat. Res. Soc. Symp. Proc. 263 (1992) 23–28.
[18] O.G. Schmidt, K. Eberl, Phys. Rev. B 61 (2000) 13721;
O.G. Schmidt, K. Eberl, A. Rau, Phys. Rev. B 62 (2000) 16715.
[19] G. Ortner, M. Bayer, A. Larionov, V.B. Timofeev, A. Forchel, Y.B. Lyanda-Geller, T.L. Reinecke, P. Hawrylak, S. Fafard, Z. Wasilewski, Phys. Rev. Lett. 90 (2003) 086404.
[20] I. Shtrichman, C. Metzner, B.D. Gerardot, W.V. Schoenfeld, P.M. Petroff, Phys. Rev. B 65 (2002) 081303.
[21] M. Bayer, P. Hawrylak, K. Hinzer, S. Fafard, M. Korkusinski, Z.R. Wasilewski, O. Stern, A. Forchel, Science 291 (2001) 451.
[22] See, e.g., P.M. Petroff, A. Lorke, A. Imamoglu, Phys. Today 54/4 (2001) 46, and references therein.
[23] J. Tersoff, C. Teichert, M.G. Lagally, Phys. Rev. Lett. 76 (1996) 1675.
[24] F. Liu, S.E. Davenport, H.M. Evans, M.G. Lagally, Phys. Rev. Lett. 82 (1999) 2528.
[25] M. Pinczolits, Springholz, G. Bauer, Phys. Rev. B 60 (1999) 11524.
[26] G.S. Solomon, S. Komarov, J.S. Harris, Y. Yamamoto, J. Cryst. Growth 175/176 (1997) 707.
[27] P. Schittenhelm, C. Engel, F. Findeis, G. Abstreiter, A.A. Darhuber, G. Bauer, A.O. Kosogov, P. Werner, J. Vac. Sci. Technol. B 16 (1998) 1575.
[28] O. Kienzle, F. Ernst, M. Rühle, O.G. Schmidt, K. Eberl, Appl. Phys. Lett. 74 (1999) 269.
[29] E. Mateeva, P. Sutter, J.C. Bean, M.G. Lagally, Appl. Phys. Lett. 71 (1997) 3233.
[30] A. Darhuber, P. Schittenhelm, V. Holy, J. Stangl, G. Bauer, G. Abstreiter, Phys. Rev. B 55 (1997) 15652.
[31] L. Goldstein, F. Glas, J.Y. Marzin, M.N. Charasse, G. Le Roux, Appl. Phys. Lett. 47 (1985) 1099.
[32] S. Guha, A. Madhukar, K.C. Rajkumar, Appl. Phys. Lett. 57 (1990) 2110.
[33] A. Darhuber, V. Holy, J. Stangl, G. Bauer, A. Krost, F. Heinrichsdorff, M. Grundmann, D. Bimberg, V.M. Ustinov, P.S. Kop'ev, A.O. Kosogov, P. Werner, Appl. Phys. Lett. 70 (1997) 955.
[34] B. Legrand, J.P. Nys, B. Grandidier, D. Stievenard, A. Lemaitre, J.M. Gerard, V. Thierry-Mieg, Appl. Phys. Lett. 74 (1999) 2608.

[35] M. Strassburg, V. Kutzer, U.W. Pohl, A. Hoffmann, I. Broser, N.N. Ledentsov, D. Bimberg, A. Rosenauer, U. Fischer, D. Gerthsen, I.L. Krestnikov, M.V. Maximov, P.S. Kop'ev, Zh.I. Alverov, Appl. Phys. Lett. 72 (1998) 942.
[36] L. Krestnikov, M. Straßburg, M. Caesar, A. Hoffmann, U.W. Pohl, D. Bimberg, N.N. Ledentsov, P.S. Kop'ev, Zh.I. Alferov, D. Litvinov, A. Rosenauer, D. Gerthsen, Phys. Rev. B 60 (1999) 8695.
[37] G. Mackowski, G. Karczewski, T. Wojtowicz, J. Kossut, S. Kret, A. Szczepanska, P. Duczewski, G. Prechtl, W. Heiss, Appl. Phys. Lett. 78 (2001) 3884.
[38] G. Springholz, M. Pinczolits, P. Mayer, V. Holy, G. Bauer, H.H. Kang, L. Salamanca-Riba, Phys. Rev. Lett. 84 (2000) 4669.
[39] G. Springholz, A. Raab, R.T. Lechner, V. Holy, Appl. Phys. Lett. 82 (2003) 799.
[40] V. Holy, G. Springholz, M. Pinczolits, G. Bauer, Phys. Rev. Lett. 83 (1999) 356.
[41] V.A. Shchukin, D. Bimberg, V.G. Malyshkin, N.N. Ledentsov, Phys. Rev. B 57 (1998) 12262.
[42] A. Raab, G. Springholz, R.T. Lechner, Phys. Rev. B 67 (2003) 165321.
[43] H. Li, J. Wu, Z. Wang, T. Daniels-Race, Appl. Phys. Lett. 75 (1999) 1173.
[44] J. Wu, Y.P. Zeng, Z.Z. Sun, F. Lin, B. Xu, Z.G. Wang, J. Cryst. Growth 21 (2000) 1803.
[45] J. Brault, M. Gendry, O. Marty, M. Pitaval, J. Olivares, G. Grenet, G. Hollinger, Appl. Surf. Sci. 162–163 (2000) 584.
[46] B. Salem, G. Brèmond, M. Hjiri, F. Hassen, H. Maaref, O. Marty, J. Brault, M. Gendry, Mater. Sci. Engrg. B 101 (2003) 259.
[47] C. Priester, G. Grenet, Phys. Rev. B 64 (2001) 125312.
[48] A. Raab, R.T. Lechner, G. Springholz, Appl. Phys. Lett. 80 (2002) 1273.
[49] W. Wu, J.R. Tucker, G.S. Solomon, J.S. Harris Jr., Appl. Phys. Lett. 71 (1997) 1083.
[50] Vinh Le Thanh, V. Yam, P. Boucaud, F. Fortune, C. Ulysse, D. Bouchier, L. Vervoort, J.-M. Lourtioz, Phys. Rev. B 60 (1999) 5851.
[51] G.S. Solomon, S. Komarov, J.S. Harris Jr., J. Cryst. Growth 201–202 (1999) 1190.
[52] O.G. Schmidt, O. Kienzle, Y. Hao, K. Eberl, F. Ernst, Appl. Phys. Lett. 74 (1999) 1272.
[53] Y. Nakata, Y. Sugiyama, T. Fuatsugi, N. Yokoyama, J. Cryst. Growth 175/176 (1997) 713.
[54] Vinh Le Thanh, V. Yam, L.H. Nguyen, Y. Zheng, P. Boucaud, D. Débarre, D. Bouchier, J. Vac. Sci. Technol. B 20 (2002) 1259.
[55] P. Sutter, E. Mateeva-Sutter, L. Vescan, Appl. Phys. Lett.78 (2001) 1736.
[56] M.K. Zundel, P. Specht, K. Eberl, N.Y. Jin-Philipp, F. Philipp, Appl. Phys. Lett. 71 (1997) 2972.
[57] J.L. Rouviere, J. Simon, N. Pelekanos, B. Daudin, G. Feullet, Appl. Phys. Lett. 75 (1999) 2632.
[58] See, e.g., S.M. Hu, J. Appl. Phys. 66 (1989) 2741;
or A.A. Maradudin, R.F. Wallis, Surf. Sci. 91 (1980) 423.
[59] J. Stangl, V. Holy, G. Bauer, Rev. Mod. Phys. 76 (2004) 725.
[60] M.A. Krivoglaz, X-Ray and Neutron Scattering in Nonideal Crystals, vol. I, Springer, Berlin, 1996.
[61] H. Li, T. Daniels-Race, M.-A. Hasan, J. Vac. Sci. Technol. B 19 (2001) 1471.
[62] H. Li, T. Daniels-Race, M.-A. Hasan, Appl. Phys. Lett. 80 (2002) 1367.
[63] H. Heidemeyer, U. Denker, C. Müller, O.G. Schmidt, Phys. Rev. Lett. 91 (2003) 196103.
[64] Y.W. Mo, D.E. Savage, B.S. Schwartzentruber, M.G. Lagally, Phys. Rev. Lett. 65 (1990) 1020.
[65] M.A. Lutz, R.M. Feenstra, P.M. Mooney, J. Tersoff, O.J. Chu, Surf. Sci. 316 (1993) L1075.
[66] G. Medeiros-Ribeiro, A.M. Bratkovski, T.I. Kamins, D.A.A. Ohlberg, R.S. Williams, Science 279 (1998) 353.
[67] F.M. Ross, R.M. Tromp, M.C. Reuter, Science 286 (1999) 1931.
[68] J. Marquez, L. Geelhaar, K. Jacobi, Appl. Phys. Lett. 78 (2001) 2309.
[69] M. Pinczolits, G. Springholz, G. Bauer, J. Cryst. Growth 201/202 (1999) 1126;
M. Pinczolits, G. Springholz, G. Bauer, Appl. Phys. Lett. 73 (1998) 250.
[70] Z. Zhong, A. Halilovic, T. Fromherz, F. Schäffler, G. Bauer, Appl. Phys. Lett. 82 (2003) 4779;
Z. Zhong, G. Bauer, Appl. Phys. Lett. 84 (2004) 1922.
[71] R. Songmuang, S. Kiravittaya, O.G. Schmidt, Appl. Phys. Lett. 82 (2003) 2892.
[72] J.M. García, G. Medeiros-Ribeiro, K. Schmidt, T. Ngo, J.L. Feng, A. Lorke, J. Kotthaus, P.M. Petroff, Appl. Phys. Lett. 71 (1997) 2014.
[73] T. Raz, D. Ritter, G. Bahir, Appl. Phys. Lett. 82 (2003) 1706.
[74] O.G. Schmidt, N.Y.J. Phillipp, C. Lange, U. Denker, K. Eberl, R. Schreiner, H. Gräbeldinger, H. Schweizer, Appl. Phys. Lett. 77 (2000) 4139.
[75] D.S.L. Mui, D. Leonard, L.A. Coldren, P.M. Petroff, Appl. Phys. Lett. 66 (1995) 1620.
[76] H. Lee, J.A. Johnson, M.Y. He, J.S. Speck, P.M. Petroff, Appl. Phys. Lett. 78 (2001) 105.
[77] R.L. Williams, G.C. Aers, P.J. Poole, J. Lefebvre, D. Chithrani, B. Lamontagne, J. Cryst. Growth 223 (2001) 321.
[78] T. Kitajima, B. Liu, S.R. Leone, Appl. Phys. Lett. 80 (2002) 497.
[79] E. Tevaarwerk, P. Rugheimer, O.M. Castellini, D.G. Keppel, S.T. Utley, D.E. Savage, M.G. Lagally, M.A. Eriksson, Appl. Phys. Lett. 80 (2002) 4626.
[80] A. Fantini, F. Phillipp, C. Kohler, J. Porsche, F. Scholz, J. Cryst. Growth 244 (2002) 129.
[81] H.R. Gutierrez, M.A. Cotta, M.M.G. de Carvalho, J. Cryst. Growth 254 (2003) 1.
[82] Z.G. Wang, J. Wu, Microelectron. J. 34 (2003) 379.
[83] See, e.g., M. Horn-von-Hoegen, Appl. Phys. A 59 (1994) 503;
E. Tournie, N. Grandjean, A. Trampert, J. Massies, K. Ploog, J. Cryst. Growth 150 (1995) 460.
[84] A. Zunger, S. Mahajan, in: T.S. Moss, S. Mahajan (Eds.), Handbook on Semiconductors, vol. 3, Elsevier Science, Amsterdam, 1994, p. 1399.
[85] C. Priester, G. Grenet, Phys. Rev. B 61 (2000) 16029.

[86] J.E. Guyer, P.W. Voorhees, Phys. Rev. Lett. 74 (1995) 4031;
J.E. Guyer, P.W. Voorhees, Phys. Rev. B 54 (1996) 11710.
[87] J. Tersoff, Phys. Rev. Lett. 77 (1996) 2017;
B.J. Spencer, P.W. Voorhees, J. Tersoff, Phys. Rev. Lett. 84 (2000) 2449.
[88] G. Springholz, M. Pinczolitsa, V. Holy, S. Zerlautha, I. Vavra, G. Bauer, Physica E 9 (2001) 149.
[89] C. Teichert, Phys. Rep. 365 (2002) 335.